

# 1 The variability of antidune morphodynamics on steep 2 slopes

3 Ivan Pascal<sup>1,\*</sup>, Christophe Ancey<sup>1</sup>, and Patricio Bohorquez<sup>2</sup>

4 <sup>1</sup>Laboratoire Hydraulique Environnementale, École Polytechnique Fédérale de Lausanne, 1015 Lausanne,  
5 Switzerland

6 <sup>2</sup>Centro de Estudios Avanzados en Ciencias de la Tierra, Universidad de Jaén, Campus de las Lagunillas, 23071  
7 Jaén, Spain

8 \*corresponding author: ivan.pascal@epfl.ch

## 9 ABSTRACT

10 Steep streams on rough beds are generally characterised by supercritical flow conditions under which antidunes  
11 can develop and migrate over time. In this paper, we present flume experiments that we conducted to investigate  
12 the variability of antidune geometry and migration celerity, a variability observed even under steady-state conditions.  
13 Quantifying this variability is important for river morphodynamics, hydraulics and paleohydraulics. We imposed  
14 moderate to intense bedload transport rates at the flume inlet in order to assess their effects on antidune mor-  
15 phodynamics for near-constant values of the mean bed slope. The bed elevation profile was monitored for each  
16 experiment with high spatial and temporal resolution. Upstream migrating antidunes were observed along most of  
17 the flume length. Considering single values for wavelength and celerity was not sufficient to describe the antidune  
18 behaviour in these experiments. By using spectral analysis, we identified the variability ranges of bedform shape  
19 and celerity. Interestingly, migration celerity increased with increasing antidune wavelength; the opposite trend  
20 was reported for dunes in other studies. Antidunes were more uniform and migrated faster for higher sediment  
21 feeding rates. Scaling the spectra made it possible to find a general dimensionless relationship between antidune  
22 wavelength and celerity. This framework provides a novel method for estimating the mean bedload transport rate in  
23 the presence of upstream migrating antidunes.

24 **Keywords:** Antidune, Bedform variability, River morphodynamics, Bedload transport, Paleohydraulics, Flume

26 **Introduction**

27 In nature, riverbeds usually exhibit bedforms of various spatial and temporal scales, which can migrate over time.

28 The occurrence of a given bed morphology depends on the hydrodynamical and sedimentary conditions (sediment

29 properties, supply, etc.). Studying bedform dynamics is important to understand both the evolution of alluvial

30 environments and the implications for flow resistance and sediment fluxes. Antidunes are bedforms typical of

31 supercritical (or near critical) flows on steep slopes and can be observed also for upper-flow regimes on mild slopes.

32 The term “antidune” was originally proposed by [Gilbert and Murphy \(1914\)](#) to identify two-dimensional bedforms that

33 migrate upstream, contrary to dunes. Nowadays, antidunes are defined as sinusoidal shaped bedforms for which

34 the water surface is in phase with the bed undulations, according to [Kennedy \(1961\)](#). This definition is adopted

35 in the present paper. Antidunes are associated with step-pool morphologies ([Whittaker and Jaeggi, 1982](#); [Grant,](#)

36 [1994](#); [Chin, 1999](#)) and may co-exist with cyclic steps in transcritical flows ([Alexander, 2008](#); [Cartigny et al., 2014](#);

37 [Slootman and Cartigny, 2020](#)). Since the pioneering work by [Kennedy \(1961, 1963, 1969\)](#), great efforts have been

38 dedicated to studying antidune formation and their stability domains (e.g. [Reynolds, 1965](#); [Engelund, 1970](#); [Hayashi,](#)

39 [1970](#); [Parker, 1975](#); [Coleman and Fenton, 2000](#); [Huang and Chiang, 2001](#); [Kubo and Yokokawa, 2001](#); [Carling](#)

40 [and Shvidchenko, 2002](#); [Colombini, 2004](#); [Colombini and Stocchino, 2005](#); [Deigaard, 2006](#); [Di Cristo et al., 2006](#);

41 [Colombini and Stocchino, 2008](#); [Bose and Dey, 2009](#); [Andreotti et al., 2012](#); [Colombini and Stocchino, 2012](#); [Vesipa](#)

42 [et al., 2012](#); [Greco et al., 2018](#); [Bohorquez et al., 2019](#)). In parallel, experimental studies on antidunes have been

43 performed to test theoretical and numerical frameworks and to investigate the main physical mechanisms governing

44 these bed instabilities (e.g. [Guy et al., 1966](#); [Cao, 1985](#); [Recking et al., 2009](#); [Mettra, 2014](#)). In paleohydraulic

45 studies, antidunes receive special attention because they are important proxies of hydraulic and sedimentary

46 conditions (e.g. [Shaw and Kellerhals, 1977](#); [Carling et al., 2009](#)). Also, downstream migrating antidunes were

47 early documented in experiments (e.g. [Kennedy, 1961](#)) but a criterion for antidune migration direction has been

48 formalised only recently ([Núñez-González and Martín-Vide, 2011](#)). Experimental studies have mostly focused

49 on downstream migrating bedforms (dunes and bars) than on antidunes. This likely reflects the high demand of

50 methods to quantify dune geometry and contribution to the sediment fluxes for streams on gentle slopes. To the best

51 of our knowledge, [Simons et al. \(1965\)](#) can be credited with the first framework for computing the contribution of

52 downstream migrating dunes to the mean bedload discharge. The existence of bedload transport pulses has been  
53 related to bedform migration ([Gomez et al., 1989](#)), a relationship that has been investigated in gravel-bed flumes  
54 through experimental investigations into alternate bars (e.g. [Dhont and Ancey, 2018](#); [Palucis et al., 2018](#)). When  
55 alternate bars are associated with near-critical flows, antidunes may develop locally and participate to sediment  
56 transport (see Movie S3 in [Dhont and Ancey, 2018](#)).

57 For steep slopes, [Recking et al. \(2009\)](#) considered data regarding antidunes occurrence and proposed new  
58 specific relationships for predicting the dominant wave geometry. Migrating antidunes of variable wavelength have  
59 been observed in gravel-bed rivers (see Video Clip S2 in [Froude et al., 2017](#)). In his flume experiments on steep  
60 slopes, [Mettra \(2014\)](#) observed antidunes characterised by varying shapes and migration celerities and investigated  
61 the contribution of upstream migrating antidunes to the bedload flux. Based on the model proposed by [Simons  
62 et al. \(1965\)](#), he proposed two expressions for estimating the mean and maximum local bedload transport rates  
63 (involving mean and maximum values of antidune amplitude and celerity). [Ancey and Pascal \(2020\)](#) monitored  
64 bedload transport in a narrow flume in presence of upstream migrating antidunes and reported bedload pulses  
65 whose period was consistent with the antidune migration period. As far as we know, an integral relationship for  
66 computing the sediment flux associated to upstream migrating antidunes is not yet available. This expression should  
67 also include the potential scale dependencies between wave geometry and migration celerity. Upstream migrating  
68 antidunes travel in the opposite direction of the bedload flux which cannot be decomposed straightforwardly in a  
69 fraction that participates to the migration of a given antidune and in a passive fraction. This peculiarity prevents the  
70 direct application of the integration frameworks already defined for downstream migrating dunes by [Nikora \(1984\)](#)  
71 and [Guala et al. \(2014\)](#).

72 Running well-controlled flume experiments provides useful insights into the bedform dynamics under steady-  
73 state conditions. We performed experiments in a steep flume in which we monitored the bed topography with high  
74 spatial and temporal resolution. We used spectral analysis to quantify the variability of antidune geometry and  
75 celerity. We analysed how sediment transport rates depended on antidune migration celerity, and how antidune  
76 variability affected in turn bedload transport. We present the outcomes of this analysis with an emphasis given to  
77 antidune wavelength and migration celerity. We provide tentative answers to the two following questions: (i) Does  
78 the variability of antidune geometry and migration celerity follow a general trend? (ii) Is it possible to define a method  
79 for estimating the mean bedload transport rate associated with upstream migrating antidunes on steep slopes?

80 The findings are discussed and their potential implications for river morphodynamics, steep-stream hydraulics and  
81 paleohydraulics are outlined.

## 82 **Methods**

### 83 **Experimental arrangement**

84 To investigate antidune morphodynamics, we carried out experiments in a 2.5-m-long 4-cm-wide flume with  
85 transparent sidewalls. We used natural gravel with median particle diameter  $d_{50} = 2.9$  mm ( $d_{16} = 2.5$  mm,  $d_{84} =$   
86 3.3 mm) and sediment density  $\rho_s = 2550$  kg m<sup>-3</sup>. The bed layer thickness was 4 cm on average. We chose  
87 well-sorted natural gravel to avoid grain sorting. This choice also had the advantage of simplifying the protocol of  
88 bedload transport rate measurement. The flume (see Figure 1) was equipped with a sediment feeder, whose supply  
89 rate was controlled by a hopper and a rotating wheel. A high-speed camera was mounted over the flume outlet to  
90 monitor the sediment discharge. Another camera was used to film bed evolution from the side. We set the flume  
91 width at 4 cm to ensure a reasonable trade-off between ease of data acquisition and representativeness of flow  
92 and morphodynamic conditions (relative to those observed in real-world scenarios). This configuration enables the  
93 accurate assessment of the quasi-equilibrium state before starting topography data collection and after the run.  
94 This condition is fundamental to guarantee that the time series of the bed topography is not significantly influenced  
95 from processes related to bed disequilibrium at the flume scale. On the other hand, running experiments in small  
96 flumes requires particular attention and accurate systems to control and assess sediment and water supply (see the  
97 last part of the next section for details). As the flow conditions and associated bedforms (antidunes in our case)  
98 were nearly two-dimensional, we could use simple imaging techniques for extracting bed topography data from side  
99 images. The  $d_{50}/W$  ratio was kept under 0.1 to mitigate lateral confinement effects.

### 100 **Experimental conditions**

101 The experiments were carried out under steady-state conditions in terms of both water discharge and sediment  
102 supply. We ran four experiments with different transport intensities and similar values of mean slope angle,  $\bar{\psi} \approx 3^\circ$   
103 (Table 1).

104 For each run, we imposed a constant sediment feed rate and set the flow discharge per unit width  $q_w$  which  
105 ensured balance between erosion and deposition at the flume scale. The sediment feed rates  $q_{s,in}$  corresponded to



different values of the ratio  $\Theta/\Theta_c$ , where  $\Theta$  is the Shields number and  $\Theta_c$  is the critical Shields number (see Table 2).

We estimated  $\Theta$  using the relationship:

$$\Theta = \frac{g\rho R_b \tan \bar{\psi}}{g(\rho_s - \rho)d_{50}} = \frac{R_b \tan \bar{\psi}}{d_{50} s - 1}, \quad (1)$$

where  $g$  is the gravitational acceleration,  $\rho$  is the water density,  $s = \rho_s/\rho$  is the sediment-to-water density ratio and  $R_b$  is the bed hydraulic radius calculated using the Einstein-Johnson sidewall correction method.

The Einstein-Johnson method (Einstein, 1942; Johnson, 1942) is based on the division of the real flow cross-section ( $h_0 \times W$ ) in one area  $A_{sw}$  dominated by the sidewall friction and one area  $A_b$  dominated by the bed friction. Two virtual parallel flumes (flow surfaces equal to  $A_{sw}$  and  $A_b$ , and rough interface lengths of  $2h_0$  and  $W$ , respectively) with the same mean flow velocity  $U$  and mean energy slope ( $\approx \bar{\psi}$ ) are then considered to compute the hydraulic radii  $R_{sw}$  and  $R_b$ . This method has proven to give a good approximation of the hydraulic features in supercritical flows in experimental flumes, also compared to more refined methods (Guo, 2015).

The hydraulic radius associated to sidewall friction  $R_{sw}$  was calculated by numerically iterating Eq. (2) and Eq. (3).

$$\frac{\tau_{sw}}{\rho} = \frac{f_{sw}}{8} U^2 = g R_{sw} \bar{\psi}. \quad (2)$$

Equation (2) is a Darcy-Weisbach-type law for the flow shearing the sidewalls where  $\tau_{sw}$  is the sidewalls' shear stress and  $f_{sw}$  is the wall friction coefficient. The latter was determined by the von-Kármán-Prandtl law as:

$$(f_{sw})^{-1/2} = 2 \log \left[ Re_{sw} (f_{sw})^{1/2} \right] - 0.8, \quad (3)$$

where  $Re_{sw} = (4UR_{sw})/\nu$  is the sidewall-related Reynolds number and  $\nu$  is the kinematic viscosity of the fluid phase.

We then computed the corresponding  $R_b$  value, according to its geometrical relationship with  $R_{sw}$ , as:

$$R_b = \frac{A_b}{W} = h_0 \left( 1 - \frac{2R_{sw}}{W} \right). \quad (4)$$

We estimated the reference flow depth  $h_0$  for the application of the Einstein-Johnson method (note that the mean flow velocity was calculated as  $U = q_w/h_0$ ) using the following Colebrook-type formula for rough fully-turbulent flows:

$$(f)^{-1/2} = -2 \log \left( \frac{d_{50}}{3.71 h_0} \right). \quad (5)$$

We decided to use a friction law to indirectly compute the reference values of  $h_0$  because determining a single representative  $h$  value in these very shallow flows requires an insidious arbitrary definition of the bed and water

surfaces. The estimated  $h_0$  values showed good consistency with the flow depth  $h$  ranges measured for each experiment using image analysis (see Table 1). Notably, the reference  $h_0$  value for each experiment was very close to the flow depth double-averaged over the control window and the entire run duration (maximum difference observed for E1, with  $\langle \bar{h} \rangle = 8.1$  mm and  $h_0 = 8.3$  mm).

Table 2 reports the critical Shields values  $\Theta_c$  estimated from the following equation proposed by Recking et al. (2008):

$$\Theta_c = 0.15(\tan \bar{\psi})^{0.275}. \quad (6)$$

Flow conditions were supercritical (see Table 2) and turbulent ( $Re = 3100 - 4800$ ) for the experiments presented here. Flows were shallow, with a relative roughness  $d_{50}/h$  in the 0.3–0.4 range.

#### ***Sediment and water supply: control and monitoring***

Since this study focused on the interplay between antidune dynamics and sediment transport conditions, particular attention was dedicated to the systems (i.e. methods and devices) used to control the sediment feeding rate and the water flow rate, and assess their stability in time.

The main components of the sediment feeder (see Figure 1) were: a sediment tank, a hopper, and a motorised wheel. The grains contained in the sediment tank descended by gravity across the hopper aperture over the wheel surface, which was covered by sandpaper. Subsequently, they were driven to falling by the wheel rotation and the coupled action of a rubber scraper, which prevented periodical avalanches. The hopper aperture was maintained constant for this experimental campaign and the sediment feeding rate was regulated by selecting the wheel angular velocity. The wheel electric motor (MODEL) was chosen during preliminary tests to ensure the desired sediment supply rates. It was important to select a motor with enough residual torque at operational angular velocities to overcome the resistance caused by grains stuck between the hopper gate and the wheel. This issue was also mitigated by adding a 5-mm-thick layer of soft foam between the cylindrical wheel and the sandpaper cover. Particular attention was given to ensuring a minimum filling level of the sediment tank (i.e. a minimum confining pressure) during each run to avoid irregularities in the granular flux inside the hopper. During their fall and before entering into the water flow, the sediments were forced to slide over an inclined white plate (illuminated by two LED spotlights) where they were filmed by a Basler acA2000-165um camera (operated at a frame rate of 100 frames per second). The videos collected during the calibration tests allowed us to compute the sediment feeding rates by

using the same method presented in this paper for the bedload transport rate monitoring at the flume outlet. The feeding rate series were compared to the sediment samples collected for different sampling durations. These tests made it possible to assess the feeder performances and identify a possible source of fluctuations in the sediment supply: the periodical grain avalanche release over the rotating wheel. This issue was fixed by installing the rubber scraper. The maximum single file size possible with this inlet monitoring setup was sufficient to collect images only for an interval of 750 s, thus the continuous monitoring of the sediment feeding during the experiments was not possible. Others possible sources of fluctuations with this sediment supply system were the misalignment of the wheel axle and the irregularities in the wheel cylindrical shape—especially in the foam coating. Therefore, these features were carefully inspected before and after each experiment. Moreover, the sediment supply rate regularity was assessed before and after each run by collecting dry sediment samples at the sediment feeder during 120–180 S.

The water recirculation was governed with a Pedrollo CP 132A pump. The flow rate was monitored using a Endress+Hauser Proline Promag 50D (DN25) electromagnetic flow-meter mounted on the delivery line (flow velocity measure range  $0.01\text{--}10\text{ m s}^{-1}$ ). The flow-meter accuracy limit was under  $1.5\%$   $Q_w$  for a total flow rate  $Q_w \geq 1.3 \cdot 10^{-4}\text{ m}^3\text{ s}^{-1}$  (that is the  $Q_w$  value for E1). The flow discharge values of the runs were lower than the nominal specifications of the recirculating pump. The flow rate was stabilised by ensuring a sufficient pressure head on the pump delivery line with a valve mounted on the piping. During the experimental runs, we also maintained a constant pressure head on the pump suction line by keeping stable the water level in the outlet reservoir. The maximum amplitude of the observed flow rate fluctuations around the mean value was smaller than  $3\%$   $Q_w$  and the fluctuation periods were shorter than 5 s. The surface water discharge values used to compute the values of the water discharge per unit width  $q_w$  (see Table 1) were obtained by subtracting the hyporheic flow discharge from the total flow rate  $Q_w$ . We measured the hyporheic flow discharge before and after each experiment by collecting manual samples at the flume outlet.

#### **Boundary conditions: specific settings**

Specific arrangements were used to set the inlet and outlet boundary conditions. We detail them here for the sake of repeatability.

The granular bed was bounded by a vertical perforated plate at the flume outlet. Similarly, a 15-cm-long plastic septum with perforated vertical walls was installed at the upstream bed boundary. Its upper face was characterised

185 by artificial roughness elements (transversal rectangular ridges  $4 \times 40 \times 2$  mm, streamwise spacing of 4 mm), whose  
186 purpose was to limit the flow velocity and thus to avoid triggering an artificial hydraulic jump at the flume inlet. The  
187 sediments were fed over this rough fixed surface in order to mitigate the sediment bursts that would have been  
188 caused by the impact of the grains over a fully mobile bed. This arrangement allowed the onset of the hyporheic  
189 flow inside the bed layer without sharp vertical deviations of the streamlines over the full bed layer. A honeycomb  
190 grid was installed upstream of both the septum and the sediment entrance to stabilise the flow free surface and  
191 mitigate the propagation of waves caused by the water inflow.

### 192 **Data collection and image processing for bed topography detection**

193 We monitored the bed topography by filming a 75-cm-long section of the flume from the side. The acquisition  
194 window was set at mid-length of the flume, with the upstream side located at  $x = 1$  m from the flume inlet ( $x = 0$  m).  
195 This central position reduced the possible influence of the boundary conditions on antidune dynamics. We collected  
196 the images of the bed profile using a Basler A504k camera (operated at a frame rate of 60 or 100 frames per  
197 second) equipped with a E Nikon lens (focal length  $f = 28$  mm, aperture in the 1–2.8 range). We processed the  
198 images (size  $1280 \times 200$  pixels, resolution 1 px = 0.6 mm) by applying a binarisation filter with a threshold level  
199 adjusted to detect the bed-water interface. We then applied a moving average filter (horizontal window of 5 px  
200  $= 3$  mm  $\simeq d_{50}$ ) to smooth small perturbations in the resulting topography caused by particles moving in the bed  
201 vicinity. The bed profile sequences were characterised by a temporal resolution of 1 s. The raw images were slightly  
202 affected by lens distortion; we decided not to correct it because the opposite effect of perspective distortion of the  
203 bed profile was intrinsic to the setup and irreparable in the present context. Therefore, the wavelength measurement  
204 accuracy on the bed profiles exceeded the camera nominal resolution and was of the order of  $d_{50}$ . To assess the  
205 wavelength accuracy, we filmed with a lateral view two thin vertical lines drawn on the opposite inner sides of each  
206 flume wall at the same cross-section (near the edge of the control window where the distortion effects are maximal)  
207 and we measured the virtual distance between these lines on the image. The maximum wavelength error estimate  
208 was approximately  $2.5 d_{50}$ .

### 209 **Bedload transport monitoring at the flume outlet**

210 We started to collect bed topography data after the system reached quasi-equilibrium between the sediment supply  
211 and the sediment discharge. To check this operational requirement, we monitored the sediment flux at the flume

outlet using a basket sampler (with a sampling time in the 60–120-s range). In addition, we filmed the particles transported by the flow over a white board placed at the flume outlet. For this monitoring system, we used the same models of camera and lens as those used for monitoring the bed topography. The  $0.055 \times 0.040$  m control window was covered by a  $190 \times 126$ -pixel frame. The frame rate was set at 60 or 100 frames per second. To estimate the bedload transport rates at the flume outlet, we used a definition based on particle activity, that is, the number of moving particles per streambed area (e.g. [Furbish et al., 2012](#)). Assuming that the mean grain velocity in the control window was constant for a given water discharge, we expressed the sediment transport rate  $q_{s,out}$  as:

$$q_{s,out}(t) = \frac{N V_b}{L W} \bar{u}_p, \quad (7)$$

where  $N(t)$  is the number of particles in the control window  $L \times W$  ( $L$  is the size in streamwise direction and  $W$  corresponds to the flume width),  $\bar{u}_p$  is the mean particle velocity in streamwise direction and  $V_b$  is the mean particle volume. It is worth noting that this equation provides the averaged transport rate over the window length  $L$ . The time resolution of the  $q_{s,out}$  series was bounded by the characteristic time that the particles took to cross the window:  $t_{tw} = L / \bar{u}_p$ . The parameters to be calculated are  $N(t)$  and  $\bar{u}_p$ . The particle activity  $N(t)$  was estimated indirectly for each image: we applied a binarisation filter to each image, and we counted the number of pixels characterised by an intensity value over a calibrated threshold. We then considered a calibration factor to convert the pixel number into the particle number  $N(t)$ . The mean velocity  $\bar{u}_p$  was estimated by tracking a set of particles (100 to 200 grains) in the control window for each experiment. During preliminary tests, we assessed that this measurement technique led to relative error in the average sediment transport rate of less than 10 % when the sampling times were in the 60–120-s range.

### Bed topography analysis

For each experiment, a bed elevation matrix  $Z_0(x, t)$  was computed from the bed profiles collected in the control window. The preliminary step towards the analysis of the bed morphodynamics involved assessing how stable the bed slope was over time. The following step consisted in the subtraction of the mean bed elevation profile from the bed elevation matrix to obtain the bed elevation perturbation matrix  $Z(x, t)$ . Each matrix  $Z(x, t)$  contained the information on the morphology and kinematics of the bedform patterns that developed and migrated during the respective run. The typical modes of the perturbations were estimated by applying a 2D Fast Fourier Transform (FFT) in the wavenumber and frequency domains to the matrix  $Z(x, t)$ . This operation was equivalent to the application

of two consecutive 1D FFT in opposite domain directions. The resulting 2D spectra were analysed to assess the variability of bedform shapes and celerities. Moreover, we tested different scaling schemes to identify general trends in these spectra.

## Results

### Bed elevation perturbations

During the experiments, antidunes developed and migrated upstream along most of the flume length. The bed topography exhibited a nearly constant mean slope over time (Figure 2).

Figure 3 shows one sample of the bed elevation perturbation matrices for each experiment. Antidune behaviour depended on the transport conditions. For example, the antidune patterns migrated more steadily during runs E2 and E3 than during E1. Generally, we observed that antidunes were more uniform and migrated faster for higher sediment feeding rates  $q_{s,in}$  (see Figure 3). During E1 and E2, antidunes were often observed to develop and migrate as groups of bedforms, also called *trains*. The number of antidunes composing each train was variable for E1 and E2. These antidune trains were occasionally disturbed or interrupted by local perturbations that propagated downstream. These downstream migrating perturbations were especially visible during E2 (Figure 3 (b)) in which they were characterised by typical spacing and period values in the ranges 0.4–0.5 m and 40–50 s respectively (perturbation velocities around 1 cm s<sup>-1</sup>). We did not observe any evidence of hydraulic jumps associated with degradation waves. The antidune sequences appeared to be mostly continuous in E3. It is interesting to note that for E4, during which it was difficult to detect antidunes in real time by simple observation, the bed patterns were visible in the corresponding  $Z(x,t)$  matrix during most of the run. The  $Z(x,t)$  matrix of E4 was characterised by a lower signal-to-noise ratio for the bed profile detection when compared to the other experiments. This signal disturbance was caused by the high particle activity in this run. For all runs, the typical antidune amplitude  $A$  ranged from the median grain size  $d_{50}$  to the mean flow depth  $h$ . The typical antidune wavelengths  $\lambda$  were approximately in the 5–15-mm range. By tracking the bedforms manually, we estimated the migration celerity  $c$  for each experiment. Due to the non-uniform migration speed, in particular for E1, the definition of a dominant celerity was considered inappropriate.

## Bedload transport rate series and fluctuations

The bedload transport rate was measured at the flume outlet throughout the time of the experiment. The resulting time series were characterised by relatively large fluctuations relative to the mean transport rates (Figure 4). Considering the transport rate series averaged over 0.2 s, the highest pulses exceeded the average transport rates by 200 % and 100 % for E1 and E4, respectively. For E1 and E2, episodes of low bedload transport ( $q_{s,out} < 10 \% \bar{q}_{s,out}$ ) at the flume outlet were also recorded. Similar episodes were not observed for E3 and E4. The overall variability of the bedload transport rates, reflected by the coefficient of variation  $C_v$ , decreased almost linearly with increasing sediment transport rates (from  $C_{v, E1} = 0.5$  to  $C_{v, E4} = 0.19$ ).

Bedload transport fluctuations at the flume outlet were likely connected with the antidune morphodynamics. For E1, the antidunes were geometrically well-developed but their migration was particularly unsteady (Figure 3 (a)). Consequently, the bedload transport rate at the flume outlet during this run exhibited high variability, reflected by the most remarkable episodes alternating intense and weak sediment transport (Figure 5). At intermediate transport stages (E2 and E3) the antidune migration was more regular (Figure 3 (b) and (c)) and the fluctuations of  $q_{s,out}(t)$  were less intermittent and less strong (Figure 5) than for E1. The bedload transport rates measured in E4 (which is the run with the highest transport intensity) showed the lowest variability, in line with earlier studies (e.g. Singh et al., 2009). The antidune signature was still noticeable in the bed elevation perturbation matrix  $Z(x, t)$  for E4 (Figure 3 (d)).

## Spectral analysis of bed morphologies

By applying the 2D Fast Fourier Transform to the  $Z(x, t)$  matrix for each experiment, we obtained the spectra shown in Figure 6 in the  $\lambda$ - $T$  domain. These spectra outlined the multi-scale nature of the bed morphologies and confirmed the observations made by considering only the bed elevation perturbation 2D plots. The FFT technique used did not allow us to determine the migration direction explicitly. In our experiments, antidunes were observed travelling upstream with non-constant geometry and migration celerity. The downstream migrating perturbations (visible in Figure 3 (b)) did not appear in these FFT spectra owing to their relatively low energy compared to those associated with the upstream migrating antidunes and their longer migration periods. Additional information regarding the downstream migrating perturbations can be found at the end of the Results section.

In order to explore and quantify variability in the antidune morphodynamics, we repeated our analysis by

considering different domains in the perturbation spectrum. In Figure 6, the Power Spectral Density (PSD) of the bed elevation perturbations in the  $\lambda$ - $T$  domain reveals wavelength variability for each experiment. The wavelength ranged from 0.05 to 0.18 cm for E1, and from 0.09 to 0.15 cm for E3. Although it was less pronounced than in similar studies on dunes (e.g. Guala et al., 2014), the wavelength variability was nonetheless noticeable in our experiments. This significant variability became less marked with increasing bedload transport intensities.

We also considered the spectra in  $c$ - $\lambda$  plane (Figure 7) in order to highlight possible trends of migration celerity. Antidune celerity was assumed to take positive values. We transformed the period values  $T$  into the corresponding migration celerity values  $c$  using the equation

$$c = \frac{\lambda}{T}. \quad (8)$$

Figure 7 shows that migration celerity increased with increasing antidune wavelength for all experiments. Otherwise stated, longer antidunes (high  $\lambda$ ) generally migrated upstream faster than shorter ones (low  $\lambda$ ). This result appeared consistent with visual analyses of the bed elevation perturbation matrices  $Z(x, t)$ . The relevance of these observations led us to analyse the spectra in dimensionless domains in order to determine how the antidune celerity depended on the problem variables. The dimensionless variables ( $T^*$ ,  $\lambda^*$ ,  $c^*$ ) were obtained by scaling the physical variables ( $T$ ,  $\lambda$ ,  $c$ ) with the reference flow depth  $h_0$  and the convective time  $\lambda/U$  as characteristic length and time, respectively:

$$T^* = T \frac{U}{\lambda}; \quad (9)$$

$$\lambda^* = \frac{\lambda}{h_0}; \quad (10)$$

$$c^* = \frac{c}{U}. \quad (11)$$

Figure 8 shows the contour plots of the spectral densities in  $c^*$ - $\lambda^*$  domain. Note the different criterion used to visualise the E4 PSD contour because this spectrum was characterised by particularly low densities. Interestingly,  $c^* \approx f(\lambda^*)$  increased with increasing  $\lambda^*$ , and the higher the transport stage, the steeper the curve  $c^* \approx f(\lambda^*)$ .

Figure 8 also indicates that experiments with the highest transport intensities were characterised by the narrowest ranges of dimensionless wavelength.



The dimensionless spectra of the various experiments did not overlap in Figure 8. We believed that the scaling based on the water phase features (see Equations (9)–(11)) did not allow us to capture the bedform dynamics in terms of dimensionless celerity and wavelength. In Figure 8, we observed that the mean sediment transport rate likely played a significant role in determining the antidune migration celerity. Based on this observation, we proposed an alternative normalisation scheme. To scale antidune celerity, we defined a characteristic sediment phase velocity  $U_N$ :

$$U_N = \frac{\bar{q}_s}{d_{V,50} (1 - p)} \quad (12)$$

where  $p$  is the porosity of the sediment mixture and  $d_{V,50}$  is a characteristic length scale for the mean particle volume  $V_b$  (i.e. the diameter of an equivalent sphere of volume  $V_b$ ). For the sediment mixture used in E1–E4, we measured  $p \simeq 0.38$  and  $d_{V,50} = (6V_b/\pi)^{1/3} \simeq 2.4$  mm.  $U_N$  is proportional to the virtual convective velocity of the sediment volume in the bed active layer—whose mean thickness was assumed proportional to the characteristic grain size. This assumption is in agreement with the typical antidune amplitude observed in our experiments. We calculated the scaled dimensionless migration celerity  $c_N^*$  as:

$$c_N^* = \frac{c}{U_N} = \frac{c d_{V,50} (1 - p)}{\bar{q}_s} \quad (13)$$

Regarding the wavelength scaling, we considered the relationship proposed by Recking et al. (2009) to predict the dominant antidune wavelength on steep slopes:

$$\lambda_{R09} = d_{50} f(\Theta, \Theta_c, Fr) = d_{50} \xi (\Theta^\alpha \Theta_c^\beta Fr^\gamma) = 0.093 \Theta \Theta_c^{-3} Fr d_{50} \quad (14)$$

The combination of parameters in Eq. (14) was the result of detailed dimensional analysis conducted using Buckingham's Pi theorem; the coefficients ( $\xi, \alpha, \beta, \gamma$ ) were determined by fitting the relationship to data derived from 19 flume experiments (Recking et al., 2009). This validated relationship appeared well-suited to be tested as the wavelength reference scale for antidunes on steep slopes. We defined the dimensionless wavelength values  $\lambda_N^*$  as:

$$\lambda_N^* = \frac{\lambda}{\xi \Theta \Theta_c^{-3} Fr d_{50}} = \frac{\lambda}{\lambda_{R09}} \quad (15)$$

The coefficient  $\xi = 0.093$  was not strictly required for the wavelength scaling but maintaining it eased the interpretation of the  $\lambda_N^*$  values in proportion to  $\lambda_{R09}$ . Figure 9 shows the resulting contour plots for the spectra in the  $c_N^*$ - $\lambda_N^*$  domain.

This scaling based on the parameters  $U_N$  and  $\lambda_{R09}$  allowed us to collapse all the spectral distributions onto a master curve  $c_N^* \approx f(\lambda_N^*)$ . The spectrum obtained for E4 followed the same trend; we plotted it separately in Figure 9b for the sake of readability. Based on the trend of the spectral distributions in Figure 9, we expressed the relationship between scaled dimensionless celerity  $c_N^*$  and dimensionless wavelength  $\lambda_N^*$  as:

$$c_N^* \approx f(\lambda_N^*) = \frac{(\lambda_N^* - \lambda_A^*)^\zeta}{k}, \quad (16)$$

where  $\lambda_A^* \simeq 0.57$  [-],  $\zeta \simeq 2/3$  [-] and  $k \simeq 1$  [-] are regression coefficients.

By combining Eq. (16) and Eq. (13), we obtained an explicit formula to estimate the mean bedload transport rate associated with upstream migrating antidunes:

$$\bar{q}_{s,est} = c d_{V,50} (1 - p) f_q(\lambda_N^*) = c d_{V,50} (1 - p) \left[ \frac{1}{(\lambda_N^* - 0.57)^{2/3}} \right], \quad (17)$$

where  $f_q(\lambda_N^*) = [f(\lambda_N^*)]^{-1}$ . Equation (17) shares some similarity with the frameworks proposed for downstream migrating dunes (e.g. Simons et al., 1965; Nikora, 1984; Guala et al., 2014) and differs in other aspects. These features are discussed in the Discussion section.

#### **Performance assessment of Equation (17) with data available in literature**

Although Eq. (17) is based on the approximation underpinning Eq. (16), it can be used to estimate the mean bedload transport rate by measuring the typical wavelength and associated celerity values for antidunes migrating upstream along steep slopes. We first assessed the performance of this approach to estimate the average bedload discharge. To that end, we used data from an experiment on antidunes obtained by Mettra (2014), who set the values listed in Table 3 for the mean bed slope  $\bar{\nu}$ , the flume width  $W$ , and the sediment size  $d_{50}$ . Mettra (2014) observed upstream migrating antidunes and applied a tracking criterion based on longitudinal bed profiles to collect wavelength and celerity data.

To run this test, we first estimated the corresponding  $\lambda_N^*$  values from the  $\lambda$  values reported in Table 3 ( $\lambda_{R09} = 0.257$  m for this experiment). The Shields number  $\Theta$  was calculated using Eq. (1) with  $R_b$  estimated according to the Einstein-Johnson method as for the experiments presented here. The critical Shields number  $\Theta_c$  was calculated using Eq. (6). We calculated the  $U_N$  and  $c_N^*$  values according to Eq. (12) and Eq. (13). Since the information about the mean particle volume was not available for the run *2deg15v*, we indirectly estimated  $d_{V,50}$  assuming the same ratio  $d_{V,50}/d_{50} = 0.83$  obtained for our experimental case. The porosity of the sediment mixture was  $p = 0.42$

(Mettra, 2014). We then used Eq. (17) to calculate the corresponding  $\bar{q}_{s,est}$  values (Table 4). Figure 10 shows the “true” positions of the pairs  $(c_N^*, \lambda_N^*)$  computed from the mean bedload transport rate  $\bar{q}_{s,meas}$  (measured during the experiment). Since the maximum relative error for the mean bedload transport estimates was less than 20 %, the outcome of the test appeared satisfactory. This test highlighted the importance of having multiple pairs  $(c, \lambda)$  or better the  $c - \lambda$  spectrum to assess and improve the reliability of the results. Unfortunately, we had to limit the comparison to a single experimental case due to the scarcity of experimental data available in the literature (in terms of associated values  $c$  and  $\lambda$ ) for antidunes on steep streams with coarse sediments.

#### **Domain of application of Equation (16) and Equation (17)**

We provide here further guidance on how to apply Equations (16) and (17). The data from which these relationships were derived came from experiments characterised by high relative roughnesses and steep slopes ( $\bar{\psi} = 3^\circ$ ). The scaling analysis presented above holds for supercritical flows over well-sorted coarse natural sediments (i.e.  $d_{50}/h \approx 0.1\text{--}0.5$  and  $d_{50} \approx 2\text{--}10$  mm). Equation (16) is valid for mean slope angles up to at least  $\bar{\psi} \sim 4^\circ$  provided the flow remains supercritical over most of the flume length and the bed shows no significant  $\psi$  fluctuations on the flume scale. Mettra (2014) observed degradation waves in one steep-slope experiment ( $\psi \approx 4^\circ$ ) and evoked the metastability of the bed profile as a potential cause. Concerning streams under near-critical flow conditions ( $Fr \gtrsim 1$ ), we recommend to carefully assess the continuity of the bed elevation perturbation field in the control window (recall Figure 3 and Figure 11) because Equation (16) is not expected to hold in presence of extensive discontinuities in the upstream migrating antidune sequences (e.g. sediment waves or transitional bedforms). During an experimental run conducted with the same flume and sediments of the present study (with  $\bar{\psi} = 1.55^\circ$  and  $Fr = 1.1$ ), Ancey and Pascal (2020) observed bed waves—characterised by “cycles of growth and decay over time scales of a few minutes, with no evidence of migration”—in the upstream part of the flume (see Movie S2 in the same paper) whilst upstream migrating antidunes were well developed in the downstream sector. A plastic plate was installed over the flow surface in the middle part of the flume to facilitate particle tracking; this disturbance probably influenced the bedforms (Ancey and Pascal, 2020). In that specific configuration, the bed morphodynamics in the upstream sector was not conform to the domain of application of Equation (16). With regards to bedload transport intensity, the experimental conditions of E4 likely represent the upper boundary when applying Eq. (17) to estimate the mean bedload transport rate. The cases characterised by very low bedload transport rates require special attention because in such circumstances, bedload transport is intermittent, and this intermittency affects antidune migration.

### About the downstream travelling perturbations

We provide here additional information regarding the downstream travelling perturbations of the antidune sequences observed in our experiments. These observations might be useful for researchers who study morphodynamic instabilities in supercritical flows. The perturbations on which we focus here (also called “disturbances” in the previous sections) were downstream travelling discontinuities or non-uniformities in the wave geometry and celerity that affected the antidune sequences in our experiments. Looking at the E2 contour plot in Figure 11, one can identify perturbations which interrupt or not the antidune pattern continuity. For instance, we observed downstream travelling perturbations which propagated from accelerating antidunes. These perturbations were often associated with the splitting of one accelerating antidune or the appearance of a transition zone—likely an area with high particle activity—in which one could not distinguish the bedform crests and troughs that were previously evident (see Figure 11). In other cases, we observed occurrences of a local slow down of one antidune that subsequently propagated downstream affecting other antidunes. The perturbations travelled with typical celerity values of the same order of magnitude of the antidune celerity. This observation suggests a strong link with the bedload transport intensity. The travelling perturbations can also be interpreted as boundaries between the antidune trains when they were long-lasting. These type of perturbations and trains were mostly evident and frequent during the experiments characterised by the lowest mean bedload transport rates (E1 and E2). Note that these trains did not vanish (or break suddenly) and apparently the flow remained supercritical over the entire flume length.

Although the width of the control window in our experiments prevented the systematic analysis of the length and time scales of these downstream travelling perturbations, our experimental setup allowed us to make some interesting observation regarding the persistence of these perturbations in the time and space domains. Sometimes, these perturbations came from upstream and travelled across the entire control window. In other cases, they seemed to be originated from a local event in the antidune sequence (e.g. the sudden acceleration of a single antidune or an antidune splitting) and they propagated downstream. We also observed travelling disturbances, which caused a marked discontinuity in the antidune pattern (i.e. the transition zones mentioned above), and that were apparently damped (diffused?) over distances of few tens of centimetres (see Figure 11).

## Discussion

As presented in the previous sections, the antidunes observed during the experimental runs exhibited significant variability of their wavelength and migration celerity. The wavelength variability was found to be less pronounced for the experiments characterised by higher mean sediment transport rate. To the best of our knowledge, the range of variability for the antidune wavelength on a steep slope under moderate and intense bedload transport conditions has so far never been specified. This result was made possible by the application of spectral analysis on high resolution data. Looking at the bed elevation perturbation profiles, the antidunes were less prone to amplitude variability. The typical antidune amplitudes were observed to be slightly smaller than the mean flow depth. Regarding the antidune migration celerity, its variability was also noticeable and antidune celerity increased with increasing wavelength. Overall, antidunes characterized by similar wavelength values migrated faster for higher mean bedload transport rate.

In the next section we discuss the factors that could cause the variability of antidune morphodynamics observed in our experiments. We then explore the potential implications for related topics such as the estimation of a friction term associated with antidunes in flows characterised by high relative roughness and the links between antidune morphodynamics and sediment transport regimes.

### Antidune morphodynamics and implications

We summarised the  $\lambda$  ranges for the experimental runs E1 to E3 in Table 5. To add an element of comparison in Table 5, we reported the wavelength  $\lambda_{\min K63}$  and  $\lambda_{R09}$  computed for each experiment.  $\lambda_{\min K63}$  is the theoretical minimum wavelength for 2D antidunes, according to Kennedy (1963), as:

$$\lambda_{\min K63} = 2\pi Fr^2 \bar{h} \quad (18)$$

As shown by Table 5, Equation (14) might provide good estimates of the mean antidune wavelength for E1 and E2. The  $\lambda_{R09}$  value estimated for E3 is closer to the maximum wavelength value. However, it is important to recall that this empirical equation was formulated to estimate the dominant antidune wavelength and its fitting was based on flume data for which the wavelength values were determined by dividing the length of the observation window by the number of antidunes detected (Recking et al., 2009).

Interestingly, the comparison of the values of  $\lambda_{\min K63}$  with the ranges of  $\lambda$  determined from the spectra indicates

that the shortest waves detected using the 2D FFT were located in the region of existence of 3D antidunes according to Kennedy's stability diagram (Kennedy, 1963). This observation indicates that upstream migrating 2D (also named *long-crested*) antidunes and 3D antidunes might co-exist and interact in supercritical flows over steep slopes contributing to the variability of antidune shapes and celerities. This speculation could be a possible interpretation for the non-linear trends of the relationship between dimensionless migration celerity and dimensionless wavelength in Figure 8 and Figure 9. The real-time observation of the flow free surface over short antidunes in our experiments revealed transversal wavelets but without evidence of roaster tails. The wave amplitude of these wavelets was noticeably smaller than that of the water surface undulations caused by the sinusoidal bedforms. Regarding the bed shape for the short antidunes in our experiments, we sporadically observed antidune troughs that were more pronounced on the flume centerline than close to the flume walls but the crests appeared 2D. These kind of short bedforms might thus be typical of very shallow supercritical flows in which the particular conditions—notably the high relative roughness—might influence their form, shaping them differently from the 3D *short-crested* antidunes reported by other authors for flows characterised by lower relative roughness values (e.g. Kennedy, 1963). The small flume width values in our study, in the experiments conducted by Mettra (2014) and in some of the runs presented by Recking et al. (2009) might also play a role on the morphodynamics of these short antidunes in terms of lateral confinement. Inoue et al. (2020) recently investigated the coexistence of 3D antidunes with alternate bars. Additional experimental studies considering different relative roughness  $d_{50}/h$  and aspect ratio  $h/W$  values—with systematic monitoring of the sediment transport and flow conditions—would be useful to further clarify the mechanisms that control the coexistence of different bedforms in supercritical flows over coarse-bedded streams.

At the meso-scale, a possible mechanism that may exacerbate variability in antidune geometry and celerity is related to the interactions within antidune trains which can involve antidunes of various wavelengths, but with similar amplitudes. These non-linear interactions often have the capacity to cause neighbouring antidunes to rearrange. Examples of this phenomenon can be observed in the contour plots of the bed elevation perturbation for E1 (see Figure 3 (a)) and E2 (see Figure 11), and in Movie V1 (see Supporting Information). Antidune interactions can be phenomenologically interpreted using the *lag distance* concept (Kennedy, 1963). Even small particle clusters eroded or deposited within a short time interval can have strong impacts on local flow and transport conditions. The effects of these perturbations are likely accentuated by the high relative roughness of the flows under study.

475 In particular, in steep streams, an increase in the particle activity can trigger collective entrainment, that is, the  
476 dislodgement of several particles at the same time (Heyman et al., 2016). Consequently, the local lag between  
477 sediment flux and shear stress can be impacted non-uniformly by these bedload bursts along the stream. As a  
478 result, antidunes exhibiting similar geometries can be perturbed, undergo a non-uniform change in their migration  
479 celerity, and coalesce (or split), producing longer (or shorter) antidunes, as was observed for instance in run E1  
480 (see Figure 3 (a) and Movie V1) and run E2 (see Figure 11). Interestingly, these events were observed mainly  
481 during E1, less frequently during E2 and were less clearly identifiable during E3 and E4. This is consistent with the  
482 fact that local bedload transport pulses (or, conversely, phases of weak transport) are more frequently observed  
483 under low bedload transport conditions than under intense transport (Singh et al., 2009).

484 The formation, development and evolution of trains composed by a number of well-developed antidunes was likely  
485 caused by the above-mentioned interactions. Similar morphological patterns have been observed in experiments  
486 and the field (e.g. Recking et al., 2009; Froude et al., 2017) and their appearance likely represents a distinctive  
487 feature of the variability of antidune morphodynamics on steep slopes. According to Grant (1994), antidune  
488 interaction within these trains promotes an increase in the antidune wavelength, which could explain step-pool  
489 formation. Similar antidune trains have also been reproduced in numerical simulations by Bohorquez and Ancyey  
490 (2016), who regarded “nonlinear coarsening” as a possible cause of the antidune wavelength increase observed in  
491 the upstream migration process.

492 The downstream travelling perturbations already described in the Results section can be interpreted as a  
493 complementary feature of the antidune trains. These disturbances either appear as the transient signature of  
494 local interactions (e.g. bedform merging and splitting events) or they mark a more persistent discontinuity in the  
495 antidune pattern and thus can be considered as boundaries between the antidune trains. We also tried to investigate  
496 the possible influences of these disturbances on the bedload transport rate series measured at the flume outlet.  
497 Assuming a constant perturbation celerity, we inferred the arrival times at the flume outlet of the perturbations that  
498 travelled across the control window. Unfortunately, we did not succeed in identifying a clear correlation between the  
499 estimated arrival times of these downstream migrating perturbations at the outlet and the occurrences of bedload  
500 pulses or phases of weak transport. The simple assumption of a constant perturbation celerity in the downstream  
501 part of the flume in which the antidunes are close to the outlet discontinuity is probably not sufficient to extrapolate a  
502 correspondence between perturbations and bedload pulses.

In our experiments of bedload transport over steep slope, antidune train morphodynamics likely depends on how particle diffusivity and deposition (governed by local flow conditions), and entrainment (strictly related to particle activity) are interrelated (Ancey and Heyman, 2014; Bohorquez and Ancey, 2016; Heyman et al., 2016). The parts played by the absolute nature of the antidune instability (Vesipa et al., 2014) and by turbulence (Breakspear, 2008) may be crucial as well. In steep stream flows under moderately intense transport conditions (as in E1 and E2), investigating these interrelations remains a great challenge because we need to: (i) track not only isolated particles, but also particle clusters when measuring particle diffusivity, (ii) run Particle Image Velocimetry (PIV) in difficult conditions, and (iii) monitor antidune evolution at high temporal and spatial resolution. Further studies on these interrelated processes are needed to confirm or infirm the possible influence of processes located far upstream (such as the sediment supply irregularities) on bedload transport in steep streams (Tucker and Bradley, 2010; Furbish and Roering, 2013; Ancey et al., 2015; Heyman et al., 2016), and their impact on bed instabilities.

Variability in the antidune morphodynamical features may affect flow resistance induced by antidunes. For flows on rough beds (that is, under low submergence conditions), the relative importance of grain- and form-induced flow resistance depends a great deal on antidune shape variability, in particular on the non-uniform and abrupt changes in bed curvature. Bed curvature alters the momentum distribution within the flow (Dressler and Yevjevich, 1984). It has been taken into account for a sinusoidal bed surface by Vesipa et al. (2012), who used the Dressler equations (Dressler, 1978)—rather than the common form of the Saint-Venant equations—and a mechanistic model for sediment transport. Our experimental results and analyses prove that form-induced flow resistance may be neglected to describe the typical bedform dynamics when one considers relatively continuous antidune trains under quasi-equilibrium transport conditions. However, the experimental observation of downstream travelling perturbations which propagated from one or two accelerating antidunes (see Figure 11) should spur further research on the interplay between curvature-induced flow resistance and antidune morphodynamics variability by taking a closer look at factors such as interaction between bedforms, the influence of the bedload transport stochastic nature, and the perturbations caused by turbulence and unsteady sediment supply.

The present study explains why antidunes are seldom directly observed in the field and possibly why geomorphological records of natural gravel-bed streams may be difficult to interpret even when antidunes were not strongly reworked by later events. Direct observation is made difficult by the antidune geometry and celerity variability, which can thus “hide” their presence during flood events. Even in field sites for which disturbing factors such as grain



sorting play a minor role, antidune trains are less visible than expected because of variability. In this respect, with the advent of cost-effective drone-based technologies (e.g. UAV-carried multi-beam sonar and ground penetrating radar) we expect a revival of interest in the field investigations on antidunes. Our experimental work is a first step towards determining the variability ranges in the antidune geometry and celerity.

### The interplay between transport intensity and upstream migration celerity

In the Results section, we demonstrated that the celerity scaling based on  $U_N$  is useful to model how the sediment flux affects the antidune migration. As expected, the larger the mean sediment flux, the higher the migration celerity  $c$ . The intense particle activity promotes deposition on the antidune stoss side, and erosion on its lee side. We now compare the structure of Eq. (17) to that of the formula (see Eq. (19)) originally proposed by [Simons et al. \(1965\)](#) to model the contribution of downstream migrating dunes to the bedload flux.

$$\bar{q}_s = (1 - p) d_{V,50} f_q(\lambda_N^*) c = \frac{1}{2} (1 - p) (2 d_{V,50}) f_q(\lambda_N^*) c \quad \text{Eq. (17)}$$

$$\bar{q}_s = \frac{1}{2} (1 - p) H_{dune} c_{dune} + C_{q,1} \quad (19)$$

As one can see in the two equations reported above, Equation (17) might also be interpreted as a “contribution” to the mean bedload flux of a triangular antidune with the same shape coefficient ( $\frac{1}{2}(1 - p)$ ) of the Simons’ formula. Analogously, the term  $2d_{V,50}$  is proportional to the bedform amplitude ( $H_{dune}$  is the dune amplitude). The migration celerities also appear in both Eq. (17) and Eq. (19). It is worth noting that the celerity of upstream migrating antidunes takes positive values in our framework whereas the sign convention is different in Eq. (19) (celerity  $c_{dune} > 0$  for downstream migrating dunes). The term  $C_{q,1}$  in Eq. (19) is a constant of integration that stands for the “part of the bedload which does not enter into propagation of dunes and ripples” (with  $C_{q,1} = 0$  at the threshold of motion and as long as the bed is covered by dunes, and  $C_{q,1} = \bar{q}_s$  in case of transport in plane bed configuration) ([Simons et al., 1965](#)). Some hypotheses concerning the possible values taken by the “shape factor” (not formally defined) were already formulated by [Mettra \(2014\)](#) for the bedload flux contribution of a single antidune. The main difference between the relationships proposed for uni- and multi-modal dune fields (e.g. [Simons et al., 1965](#); [Nikora, 1984](#); [Guala et al., 2014](#)) and Eq. (17) is that the latter should not be intended as the integral of the bedload flux contributions resulting from multiple migrating bedforms of different geometry. This semi-empirical multi-scale

relationship for estimating the mean bedload transport rate is based on Eq. (16), which can be interpreted as: an upstream migrating antidune within an antidune sequence under quasi-equilibrium transport conditions typically responds to the forcing imposed by the mean bedload transport rate  $\bar{q}_s$  by migrating with celerity proportional to  $U_N$  and to  $f(\lambda_N^*)$ . According to our results, antidune upstream migration may be formally interpreted as a response to the mean bedload flux and not as a contribution to it. The functional form of the dimensionless wavelength  $f(\lambda_N^*) = [f_q(\lambda_N^*)]^{-1}$  in Eq. (16) embeds the effects on the migration celerity of both antidune shape and mean flow conditions (see Eq. (14)). The term  $f(\lambda_N^*)$  (see Eq. (16)) can be interpreted as an empirical conversion factor that expresses the typical ratio of the mean bedload flux that actively participates in determining the migration celerity of antidunes characterised by a dimensionless wavelength  $\lambda_N^*$  (depositing on their stoss side and being eroded by their lee side). The positive trend for  $f(\lambda_N^*)$  likely reflects the signature of the damping effect induced by the bedload layer inertia on antidune migration. In fact, inertial effect can increase the lag between sediment flux and shear stress, slowing antidune migration. The negative impact of inertia on the antidune migration celerity has been demonstrated theoretically by Vesipa et al. (2012). It seems coherent that this damping effect impacts relatively more the migration celerity of the short antidunes than that of the long ones because of their different size, thus causing the non-linearity in  $f(\lambda_N^*)$ . According to our observations, the interplay between sediment flux and inertia may hold at relatively high transport rates (E4) until to the situation in which the antidunes are levelled out (bedload-laden flow with not clearly identifiable bed-flow interface). Considering the PSD countour for E1 in Fig. 9a,  $f(\lambda_N^*)$  may take values higher than the unity. This somewhat unexpected outcome might suggest that the longest antidunes during E1 migrated under sustained bedload transport rate higher than the mean feeding rate (i.e. during long-lasting bedload pulses) and/or that their actual wave amplitude was lower than  $2d_{V,50}$ . However, in our experiments we did not find any clear proportionality between the antidune amplitude and wavelength. It is worth underlining that the scaling method presented in this paper is based on parameters that have been estimated by considering relationships holding for uniform flows. This method has proven to be successful for describing the typical morphodynamic features observed in our experiments; alternative approaches, which take flow non-uniformity into account, could reveal interesting information concerning particular local events such as bedload pulses associated to the migration of a single antidune or to the transit of a downstream travelling perturbation.

## Conclusion

The experimental study presented in this paper shows that antidunes on steep slopes exhibit significant variability of shapes and celerity, even under steady-state conditions. The wavelength variability range increased with decreasing mean sediment transport rate. Overall, we observed that the larger the antidune wavelength, the higher its migration celerity. One strength of this paper is to show how to infer information on this variability from high resolution data by applying spectral analysis. By using a scaling technique, we collapsed all the bed elevation perturbation spectra onto a single curve that captured the bedform dynamics in terms of dimensionless celerity  $c_N^*$  and wavelength  $\lambda_N^*$ . The resulting trend  $c_N^* \approx f(\lambda_N^*)$  was described by a functional relationship. This multi-scale relationship embedded the interplay between the sediment flux and antidune migration. We proposed a new method for estimating the mean bedload transport rate by monitoring antidune morphodynamics. Although our first test gave satisfactory results, additional data are needed to confirm our results. We are currently conducting a new experimental campaign using a longer flume.

Accounting for variability in the antidune morphodynamical features is key to estimating sediment fluxes and form-induced flow resistance on steep slopes. This variability likely explains the elusiveness of antidunes in direct field observations. The findings may help paleohydraulics studies regarding coarse-bedded streams.

## Acknowledgements

P.B. was supported by the Spanish Ministry of Science, Innovation and Universities (MICINN/FEDER, UE) under Grant CGL2015-70736-R. We thank Dr. François Mettra for all discussions related to his data. Note also that he built the former version of the flume that we used for our experiments. We thank Gaëtan Gindrat for his contribution to the experimental work during his semester project with us. We are grateful to Dr. Gauthier Rousseau for the fruitful exchanges concerning the experimental setup.

## Conflict of interest

The authors declare that there is no conflict of interest that might be perceived as influencing the authors' objectivity and the impartiality of the research presented.

## Data availability statement

The data that support the findings of this study are available in the supplementary material of this article. Bed topography data are available in Supporting Information D1. Bedload transport data are available in Supporting Information D2.

## References

- Alexander, J. (2008). Bedforms in froude-supercritical flow. In *Marine and River Dune Dynamics*, pages 1–5.
- Ancey, C., Bohorquez, P., and Heyman, J. (2015). Stochastic interpretation of the advection diffusion equation and its relevance to bed load transport. *Journal of Geophysical Research: Earth Surface*, 120:2529–2551.
- Ancey, C. and Heyman, J. (2014). A microstructural approach to bed load transport: mean behaviour and fluctuations of particle transport rates. *Journal of Fluid Mechanics*, 744:129–168.
- Ancey, C. and Pascal, I. (2020). Estimating mean bedload transport rates and their uncertainty. *Journal of Geophysical Research: Earth Surface*, 125:e2020JF005534.
- Andreotti, B., Claudin, P., Devauchelle, O., Durán, O., and Fourrière, A. (2012). Bedforms in a turbulent stream: ripples, chevrons and antidunes. *Journal of Fluid Mechanics*, 690:94–128.
- Bohorquez, P. and Ancey, C. (2016). Particle diffusion in non-equilibrium bedload transport simulations. *Applied Mathematical Modelling*, 40:7474–7492.
- Bohorquez, P., Cañada Pereira, P., Jimenez-Ruiz, P., and del Moral-Erencia, J. (2019). The fascination of a shallow-water theory for the formation of megaflood-scale dunes and antidunes. *Earth-Science Reviews*, 193:91–108.
- Bose, S. K. and Dey, S. (2009). Reynolds averaged theory of turbulent shear flows over undulating beds and formation of sand waves. *Physical review E*, 80(3):036304.
- Breakspear, R. (2008). *Hydrodynamics and sedimentary structures of antidunes in gravel and sand mixtures*. PhD thesis, University of Southampton.
- Cao, H. H. (1985). *Résistance hydraulique d'un lit de gravier mobile à pente raide étude expérimentale*. PhD thesis, École Polytechnique Fédérale de Lausanne.

631 Carling, P. A., Burr, D. M., Johnsen, T. F., and Brennand, T. A. (2009). A review of open-channel megaflood  
632 depositional landforms on Earth and Mars. In Burr, D., Carling, P., and Baker, V., editors, *Megaflooding on Earth  
633 and Mars*, pages 33–49. Cambridge University Press.

634 Carling, P. A. and Shvidchenko, A. B. (2002). A consideration of the dune: antidune transition in fine gravel.  
635 *Sedimentology*, 49(6):1269–1282.

636 Cartigny, M., Ventra, D., Postma, G., and Den Berg, J. H. (2014). Morphodynamics and sedimentary structures of  
637 bedforms under supercritical-flow conditions: New insights from flume experiments. *Sedimentology*, 61:712–748.

638 Chin, A. (1999). The morphologic structure of step-pools in mountain streams. *Geomorphology*, 27(3):191–204.

639 Coleman, S. and Fenton, J. (2000). Potential-flow instability theory and alluvial stream bed forms. *Journal of Fluid  
640 Mechanics*, 418:101–117.

641 Colombini, M. (2004). Revisiting the linear theory of sand dune formation. *Journal of Fluid Mechanics*, 502:1–16.

642 Colombini, M. and Stocchino, A. (2005). Coupling or decoupling bed and flow dynamics: fast and slow sediment  
643 waves at high Froude numbers. *Physics of Fluids*, 17:036602.

644 Colombini, M. and Stocchino, A. (2008). Finite-amplitude river dunes. *Journal of Fluid Mechanics*, 611:283–306.

645 Colombini, M. and Stocchino, A. (2012). Three-dimensional river bed forms. *Journal of Fluid Mechanics*, 695:63–80.

646 Deigaard, R. (2006). Breaking antidunes: Cyclic behavior due to hysteresis. *Journal of Hydraulic Engineering*,  
647 132(6):620–623.

648 Dhont, B. and Ancey, C. (2018). Are bedload transport pulses in gravel-bed rivers created by bar migration or  
649 sediment waves? *Geophysical Research Letters*, 45:5501–5508.

650 Di Cristo, C., Iervolino, M., and Vacca, A. (2006). Linear stability analysis of a 1-D model with dynamical description  
651 of bed-load transport. *Journal of Hydraulic Research*, 44(4):480–487.

652 Dressler, R. (1978). New nonlinear shallow-flow equations with curvature. *Journal of Hydraulic Research*, 16:205–  
653 222.

654 Dressler, R. F. and Yevjevich, V. (1984). Hydraulic-resistance terms modified for the Dressler curved-flow equations.  
655 *Journal of Hydraulic Research*, 22(3):145–156.

656 Einstein, H. (1942). Formulas for the transportation of bed load. *Transactions of the American Society of Civil*  
657 *Engineers*, 107:561–597.

658 Engelund, F. (1970). Instability of erodible beds. *Journal of Fluid Mechanics*, 42:225–244.

659 Froude, M. J., Alexander, J., Barclay, J., and Cole, P. (2017). Interpreting flash flood palaeoflow parameters from  
660 antidunes and gravel lenses: An example from montserrat, west indies. *Sedimentology*, 64(7):1817–1845.

661 Furbish, D., Haff, P., Roseberry, J., and Schmeeckle, M. (2012). A probabilistic description of the bed load sediment  
662 flux: 1. Theory. *Journal of Geophysical Research*, 117:F03031.

663 Furbish, D. and Roering, J. (2013). Sediment disentrainment and the concept of local versus nonlocal transport on  
664 hillslopes. *Journal of Geophysical Research*, 118:937–952.

665 Gilbert, G. K. and Murphy, E. C. (1914). The transportation of débris by running water. Technical report, U.S.  
666 Geological Survey Professional Paper vol. 86.

667 Gomez, B., Naff, R., and Hubbell, D. (1989). Temporal variations in bedload transport rates associated with the  
668 migration of bedforms. *Earth Surface Processes and Landforms*, 14:135–156.

669 Grant, G. E. (1994). Hydraulics and sediment transport dynamics controlling step-pool formation in high gradient  
670 streams: a flume experiment. In *Dynamics and geomorphology of mountain rivers*, pages 241–250. Springer.

671 Greco, M., Iervolino, M., and Vacca, A. (2018). Analysis of bedform instability with 1-D two-phase morphodynamical  
672 models. *Advances in Water Resources*, 120:50–64.

673 Guala, M., Singh, A., BadHeartBull, N., and Foufoula-Georgiou, E. (2014). Spectral description of migrating bed  
674 forms and sediment transport. *Journal of Geophysical Research: Earth Surface*, 119:123–137.

675 Guo, J. (2015). Sidewall and non-uniformity corrections for flume experiments. *Journal of Hydraulic Research*,  
676 53(2):218–229.

677 Guy, H. P., Simons, D. B., and Richardson, E. V. (1966). *Summary of alluvial channel data from flume experiments*,  
678 1956-61, volume 462. US Government Printing Office.

679 Hayashi, T. (1970). Formation of dunes and antidunes in open channels. *Journal of the Hydraulics Division*, ASCE  
680 96 (HY2):357–366.

681 Heyman, J., Bohorquez, P., and Ancey, C. (2016). Entrainment, motion, and deposition of coarse particles  
682 transported by water over a sloping mobile bed. *Journal of Geophysical Research: Earth Surface*, 121:1931–  
683 1952.

684 Huang, L.-H. and Chiang, Y.-L. (2001). The formation of dunes, antidunes, and rapidly damping waves in alluvial  
685 channels. *International journal for numerical and analytical methods in geomechanics*, 25(7):675–690.

686 Inoue, T., Watanabe, Y., Iwasaki, T., and Otsuka, J. (2020). Three-dimensional antidunes coexisting with alternate  
687 bars. *Earth Surface Processes and Landforms*, 45(12):2897–2911.

688 Johnson, J. W. (1942). The importance of side-wall correction in bed-load investigation. *Civil Engineering*, 12(6).

689 Kennedy, J. F. (1961). *Stationary waves and antidunes in alluvial channels*. PhD thesis, California Institute of  
690 Technology.

691 Kennedy, J. F. (1963). The mechanics of dunes and antidunes in erodible-bed channels. *Journal of Fluid mechanics*,  
692 16(4):521–544.

693 Kennedy, J. F. (1969). The formation of sediment ripples, dunes, and antidunes. *Annual Review of Fluid Mechanics*,  
694 1:147–168.

695 Kubo, Y. and Yokokawa, M. (2001). *Theoretical study on breaking of waves on antidunes*. Wiley Online Library.

696 Mettra, F. (2014). *Morphodynamic mechanisms in steep channels: from local processes to large-scale evolution*.  
697 PhD thesis, École Polytechnique Fédérale de Lausanne.

698 Nikora, V. (1984). *The structure of turbulent flow and statistical characterisation of dune-covered river beds (with  
699 examples of field studies in rivers Turunchuk, Rioni, and Tsheniscali)*. PhD thesis.

700 Núñez-González, F. and Martín-Vide, J. P. (2011). Analysis of antidune migration direction. *Journal of Geophysical  
701 Research: Earth Surface*, 116(F2).

702 Palucis, M. C., Ulizio, T. P., Fuller, B., and Lamb, M. P. (2018). Flow resistance, sediment transport, and bedform  
703 development in a steep gravel-bedded river flume. *Geomorphology*, 320:111–126.

704 Parker, G. (1975). Sediment inertia as cause of river antidunes. *Journal of Hydraulic Division*, 101:211–221.

705 Recking, A., Bacchi, V., Naaïm, M., and Frey, P. (2009). Antidunes on steep slopes. *Journal of Geophysical*  
706 *Research*, 114:F04025.

707 Recking, A., Frey, P., Paquier, A., Belleudy, P., and Champagne, J. (2008). Feedback between bed load transport  
708 and flow resistance in gravel and cobble bed rivers. *Water Resources Research*, 44:W05412.

709 Reynolds, A. J. (1965). Waves on the erodible bed of an open channel. *Journal of Fluid Mechanics*, 22(1):113–133.

710 Shaw, J. and Kellerhals, R. (1977). Paleohydraulic interpretation of antidune bedforms with applications to antidunes  
711 in gravel. *Journal of Sedimentary Research*, 47(1):257–266.

712 Simons, D. B., Richardson, E. V., and Nordin, C. F. (1965). Bedload equation for ripples and dunes. Technical  
713 Report Professional Paper 462 H, U.S. Geological Survey.

714 Singh, A., Fienberg, K., Jerolmack, D., Marr, J., and Fofoula-Georgiou, E. (2009). Experimental evidence for statis-  
715 tical scaling and intermittency in sediment transport rates. *Journal of Geophysical Research*, 114:2007JF000963.

716 Slooman, A. and Cartigny, M. J. (2020). Cyclic steps: Review and aggradation-based classification. *Earth-Science*  
717 *Reviews*, 201:102949.

718 Tucker, G. and Bradley, D. (2010). Trouble with diffusion: reassessing hillslope erosion laws with a particle-based  
719 model. *Journal of Geophysical Research*, 115:F00A10.

720 Vesipa, R., Camporeale, C., and Ridolfi, L. (2012). A shallow-water theory of river bedforms in supercritical  
721 conditions. *Physics of Fluids*, 24:094104.

722 Vesipa, R., Camporeale, C., Ridolfi, L., and Chomaz, J.-M. (2014). On the convective-absolute nature of river  
723 bedform instabilities. *Physics of Fluids*, 26:124104.

724 Whittaker, J. G. and Jaeggi, M. (1982). Origin of step-pool systems in mountain streams. *Journal of the Hydraulics*  
725 *Division*, 108(6):758–773.



## List of Figures

1	Experimental setup: (a) transparent tilting flume for quasi 2D flow, (b) sediment feeding system, (c) camera for monitoring sediment supply at the inlet, (d) camera for monitoring bedload discharge at the outlet, (e) window captured by the side camera (length $L_w = 0.75$ m). . . . .	30
2	Time series of the mean bed slope in the control window for each experiment (black solid lines). Sub-plots from (a) to (d) refer to experiments from E1 to E4, respectively. The red dashed line indicates the mean bed slope over the entire duration of the experiment. . . . .	31
3	Contour plots of the bed elevation perturbation for time intervals of 250 s (from $t_1 = 1200$ s to $t_2 = 1450$ s). Sub-plots from (a) to (d) refer to experiments from E1 to E4, respectively. The colorbars refer to the $z$ perturbations expressed as [m]. Sediment feeding rates $q_{s,in}$ were: (E1) $2.0 \cdot 10^{-5} \text{ m}^2 \text{ s}^{-1}$ , (E2) $3.5 \cdot 10^{-5} \text{ m}^2 \text{ s}^{-1}$ , (E3) $4.8 \cdot 10^{-5} \text{ m}^2 \text{ s}^{-1}$ , (E4) $6.1 \cdot 10^{-5} \text{ m}^2 \text{ s}^{-1}$ . . . . .	32
4	Time series of the bedload transport rate at the flume outlet during 1000 s for experiments E1 (a) and E4 (b). The grey solid line indicates the bedload transport rate series averaged over 0.2 s. The black solid line refers to the bedload transport rate averaged over 3 s. The red dashed line indicates the bedload transport rate averaged over the entire duration of the experiment, $\bar{q}_{s,out} \simeq q_{s,in}$ . The additional dashed lines represent: $2 q_{s,in}$ (yellow), $3 q_{s,in}$ (blue), $0.10 q_{s,in}$ (purple). . . . .	33
5	Empirical probability density functions for $q_{s,out}/q_{s,in}$ for all the experiments. These distributions refer to the bedload transport rates $q_{s,out}$ averaged over 0.2 s. . . . .	34
6	Spectra displayed in $\lambda$ - $T$ domain for experiments E1–E4 (a–d). . . . .	35
7	Spectra displayed in $c$ - $\lambda$ domain for experiments E1–E4 (a–d). . . . .	36
8	PSD contour plot in $c^*$ - $\lambda^*$ domain. The colours refer to: E1 (black), E2 (red), E3 (blue), E4 (purple). Contours are defined considering a single density level of 5000 for E1–E3. The E4 contour is defined with a density level of 500. . . . .	37
9	PSD contour plots in $c_N^*$ - $\lambda_N^*$ domain. The black lines represent the master curve of Eq. (16). (a) The colours refer to: E1 (grey), E2 (red), E3 (blue). Contours are defined considering a single density level of 5000 for E1–E3. (b) The E4 contour (purple) is defined with a density level of 500. . . . .	38
10	Master curve of Eq. (16) (dashed black line). The orange circles display the positions in $c_N^*$ - $\lambda_N^*$ domain of the data pairs reported in Table 3 for the run <i>2deg15v</i> (Mettra, 2014). The pairs $(c_N^*, \lambda_N^*)$ were calculated considering the $\bar{q}_{s,meas}$ value measured by Mettra (2014) and reported in Table 4. . . . .	39
11	Contour plot of the bed elevation perturbation $Z(x, t)$ during E2 (100 s). The solid blue lines represent the approximated crest trajectory of undisturbed antidunes. The solid orange lines indicate the accelerating antidunes whereas the green lines indicate new antidune crests resulting from splitting events or disturbance-related discontinuities. The other thick lines represent: a travelling disturbance with discontinuity of the antidune pattern (long-dashed red), a splitting-related disturbance without persistent discontinuity (short-dashed red) and a secondary discontinuity/rearrangement of the antidune pattern (long-dashed yellow) associated with a previous discontinuity. The colorbar refers to the $z$ perturbation expressed as [m]. . . . .	40

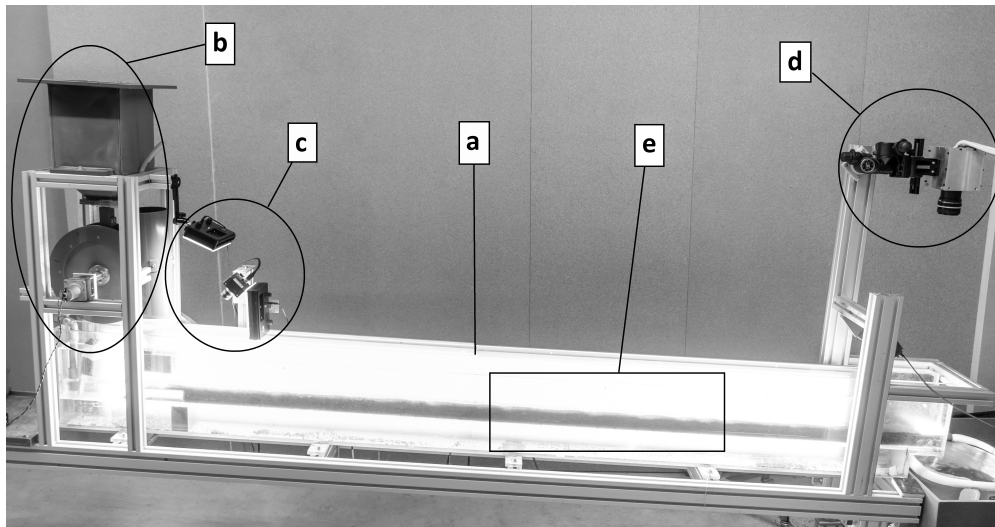


**Figure 1.** Experimental setup: (a) transparent tilting flume for quasi 2D flow, (b) sediment feeding system, (c) camera for monitoring sediment supply at the inlet, (d) camera for monitoring bedload discharge at the outlet, (e) window captured by the side camera (length  $L_w = 0.75$  m).

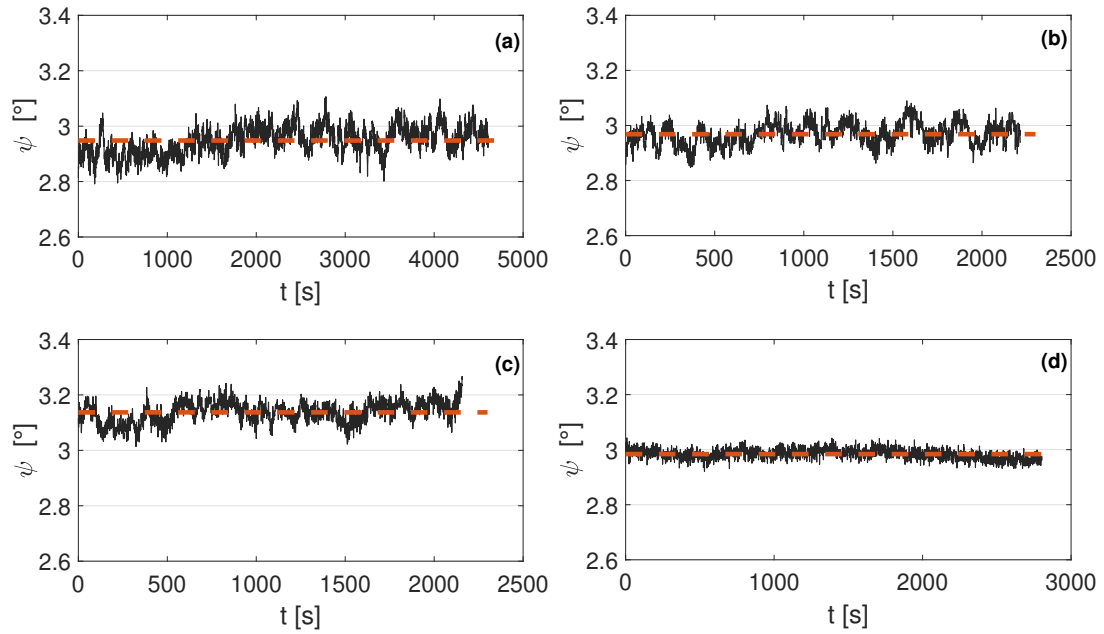


**Figure 2.** Time series of the mean bed slope in the control window for each experiment (black solid lines). Sub-plots from (a) to (d) refer to experiments from E1 to E4, respectively. The red dashed line indicates the mean bed slope over the entire duration of the experiment.

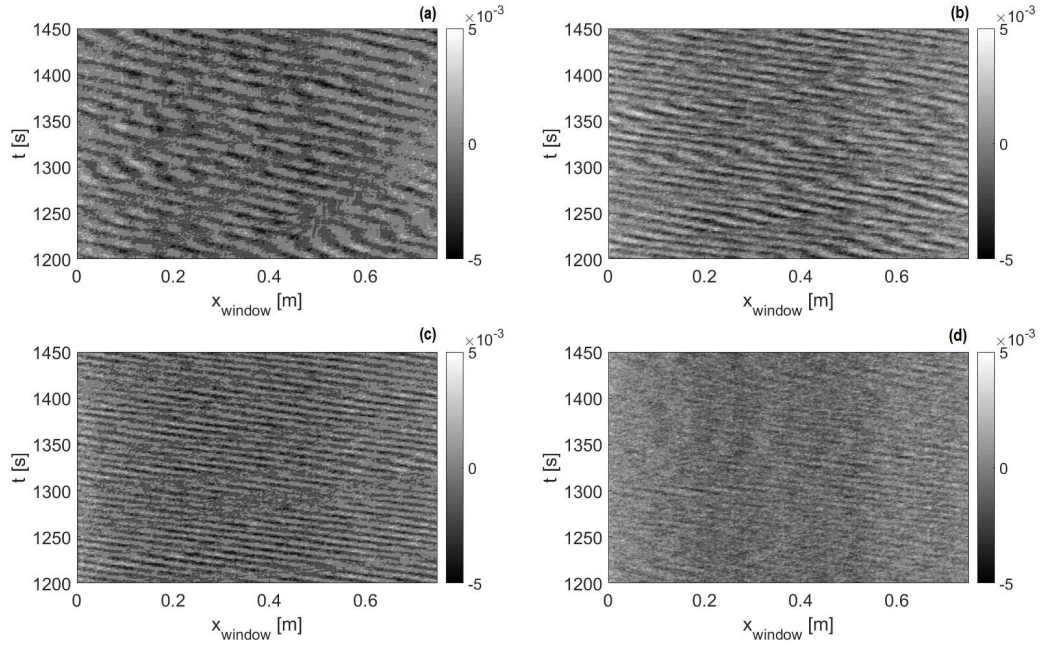


**Figure 3.** Contour plots of the bed elevation perturbation for time intervals of 250 s (from  $t_1 = 1200$  s to  $t_2 = 1450$  s). Sub-plots from (a) to (d) refer to experiments from E1 to E4, respectively. The colorbars refer to the  $z$  perturbations expressed as [m]. Sediment feeding rates  $q_{s,in}$  were: (E1)  $2.0 \cdot 10^{-5} \text{ m}^2 \text{ s}^{-1}$ , (E2)  $3.5 \cdot 10^{-5} \text{ m}^2 \text{ s}^{-1}$ , (E3)  $4.8 \cdot 10^{-5} \text{ m}^2 \text{ s}^{-1}$ , (E4)  $6.1 \cdot 10^{-5} \text{ m}^2 \text{ s}^{-1}$ .

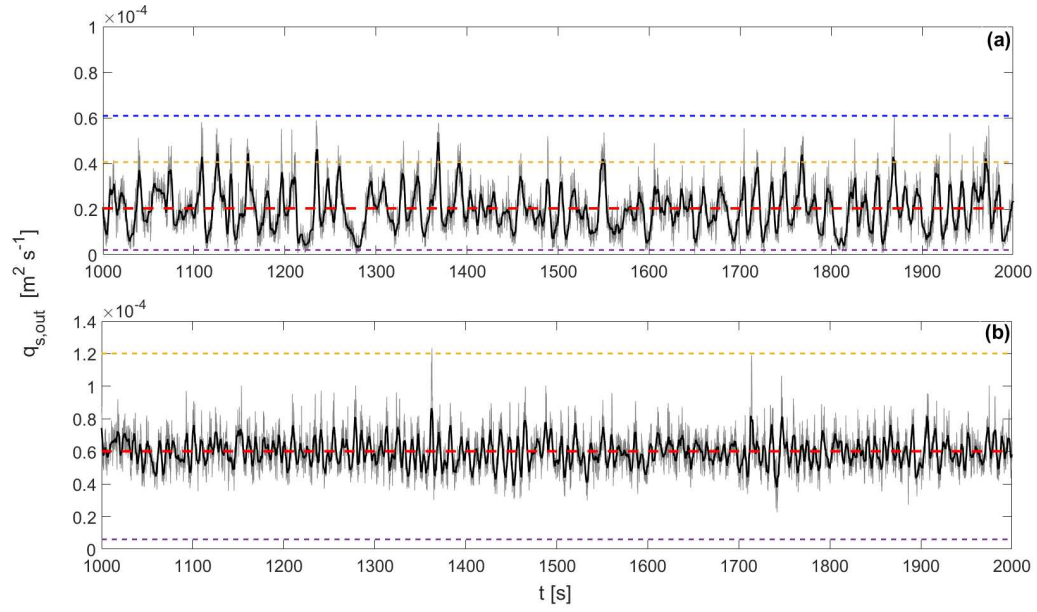


**Figure 4.** Time series of the bedload transport rate at the flume outlet during 1000 s for experiments E1 (a) and E4 (b). The grey solid line indicates the bedload transport rate series averaged over 0.2 s. The black solid line refers to the bedload transport rate averaged over 3 s. The red dashed line indicates the bedload transport rate averaged over the entire duration of the experiment,  $\bar{q}_{s,out} \simeq q_{s,in}$ . The additional dashed lines represent:  $2 q_{s,in}$  (yellow),  $3 q_{s,in}$  (blue),  $0.10 q_{s,in}$  (purple).

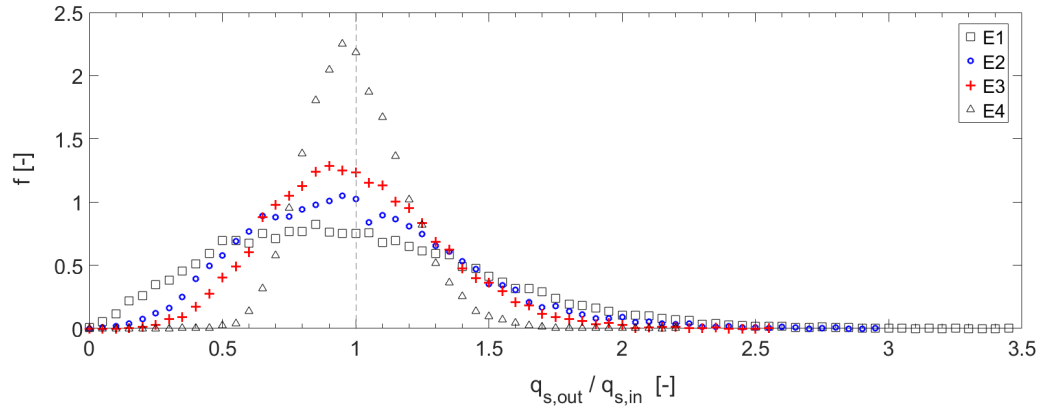


**Figure 5.** Empirical probability density functions for  $q_{s,out}/q_{s,in}$  for all the experiments. These distributions refer to the bedload transport rates  $q_{s,out}$  averaged over 0.2 s.

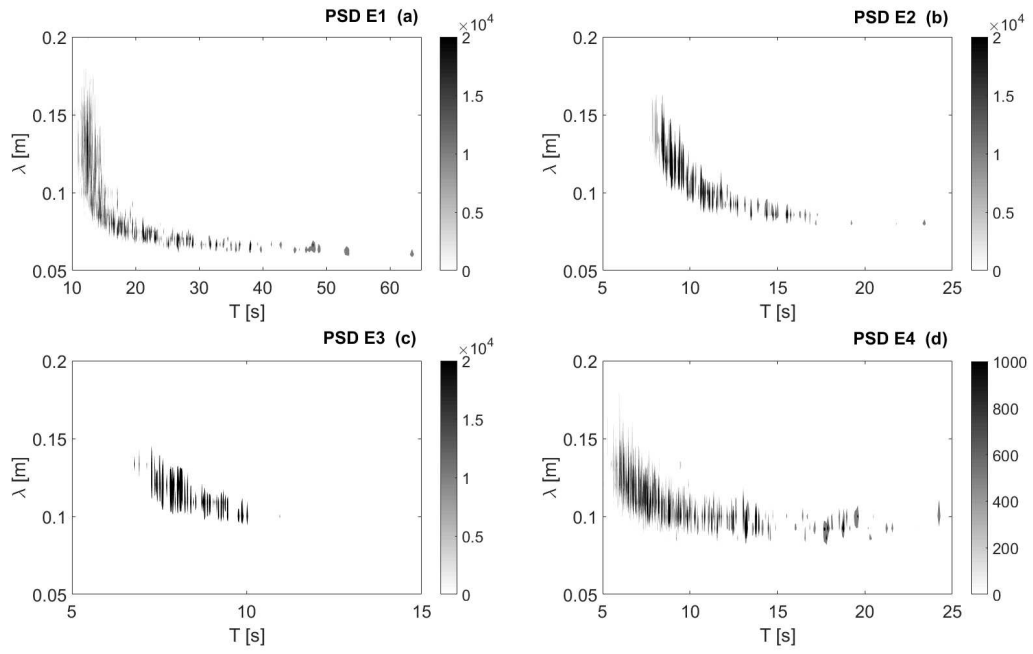


**Figure 6.** Spectra displayed in  $\lambda$ - $T$  domain for experiments E1–E4 (a–d).

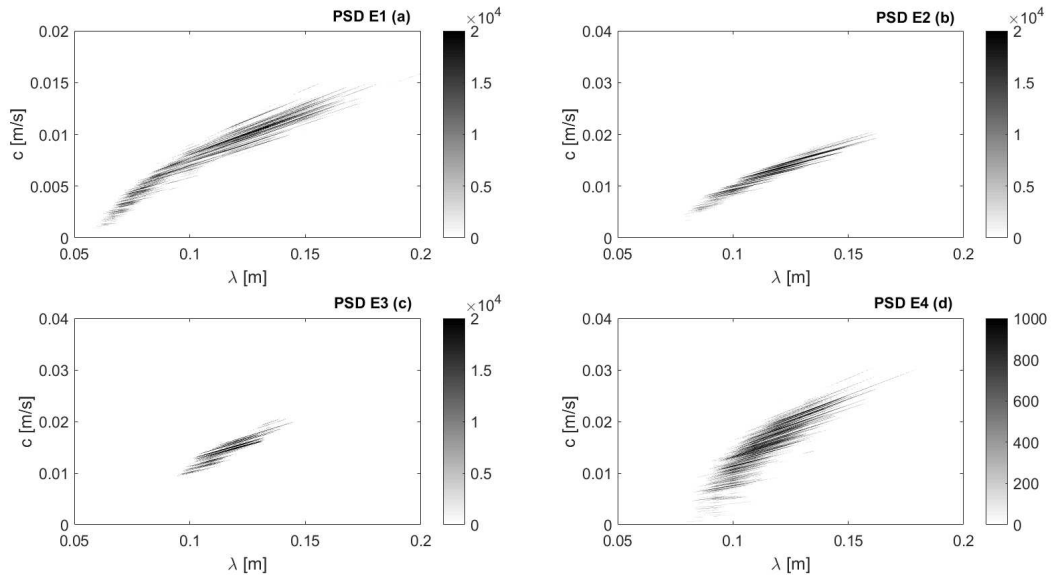


**Figure 7.** Spectra displayed in  $c$ - $\lambda$  domain for experiments E1–E4 (a–d).



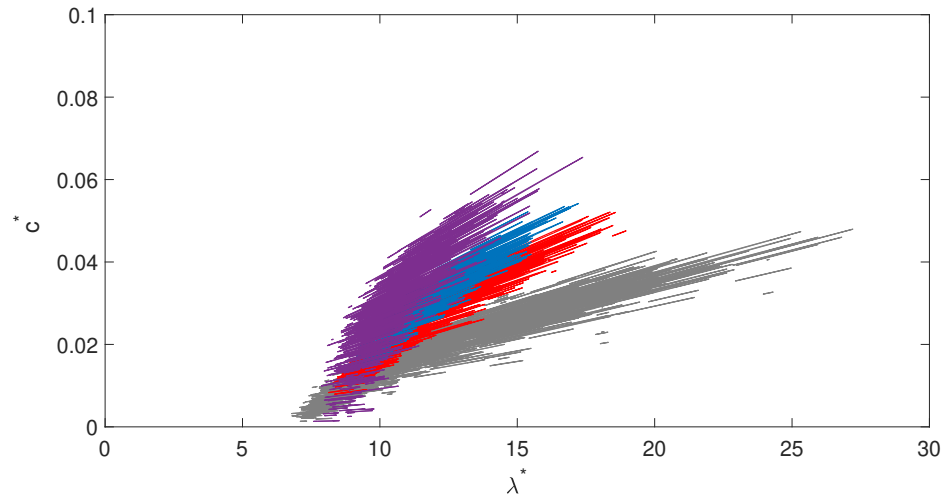


**Figure 8.** PSD contour plot in  $c^*$ - $\lambda^*$  domain. The colours refer to: E1 (black), E2 (red), E3 (blue), E4 (purple). Contours are defined considering a single density level of 5000 for E1–E3. The E4 contour is defined with a density level of 500.

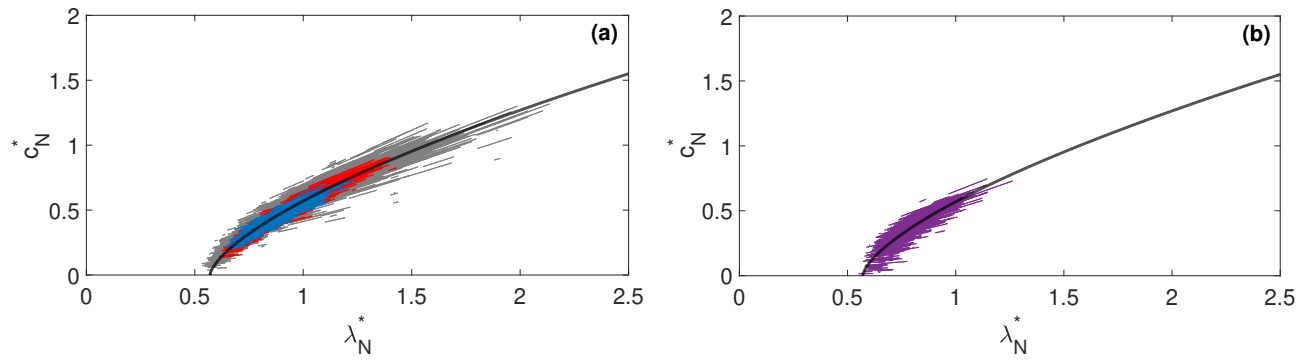


**Figure 9.** PSD contour plots in  $c_N^*$ - $\lambda_N^*$  domain. The black lines represent the master curve of Eq. (16). (a) The colours refer to: E1 (grey), E2 (red), E3 (blue). Contours are defined considering a single density level of 5000 for E1–E3. (b) The E4 contour (purple) is defined with a density level of 500.

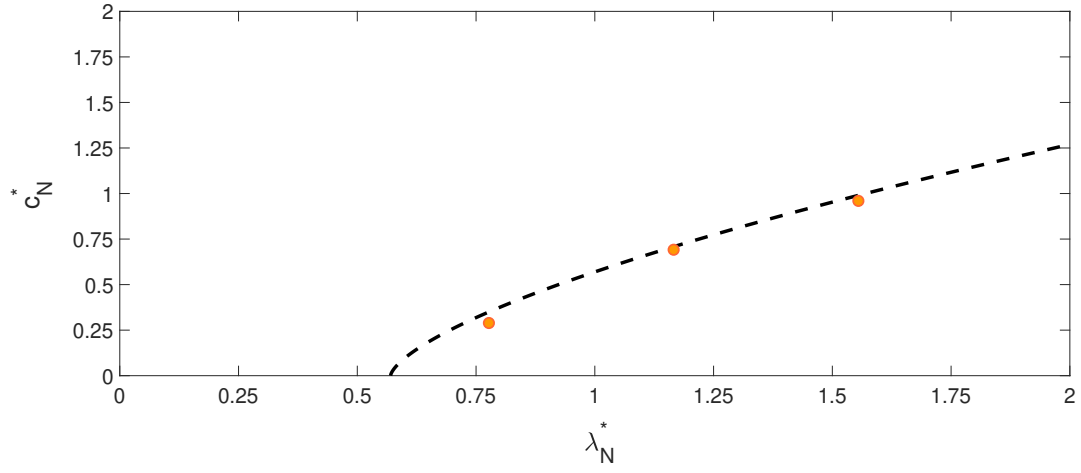


**Figure 10.** Master curve of Eq. (16) (dashed black line). The orange circles display the positions in  $c_N^*$ - $\lambda_N^*$  domain of the data pairs reported in Table 3 for the run *2deg15v* (Mettra, 2014). The pairs  $(c_N^*, \lambda_N^*)$  were calculated considering the  $\bar{q}_{s, meas}$  value measured by Mettra (2014) and reported in Table 4.

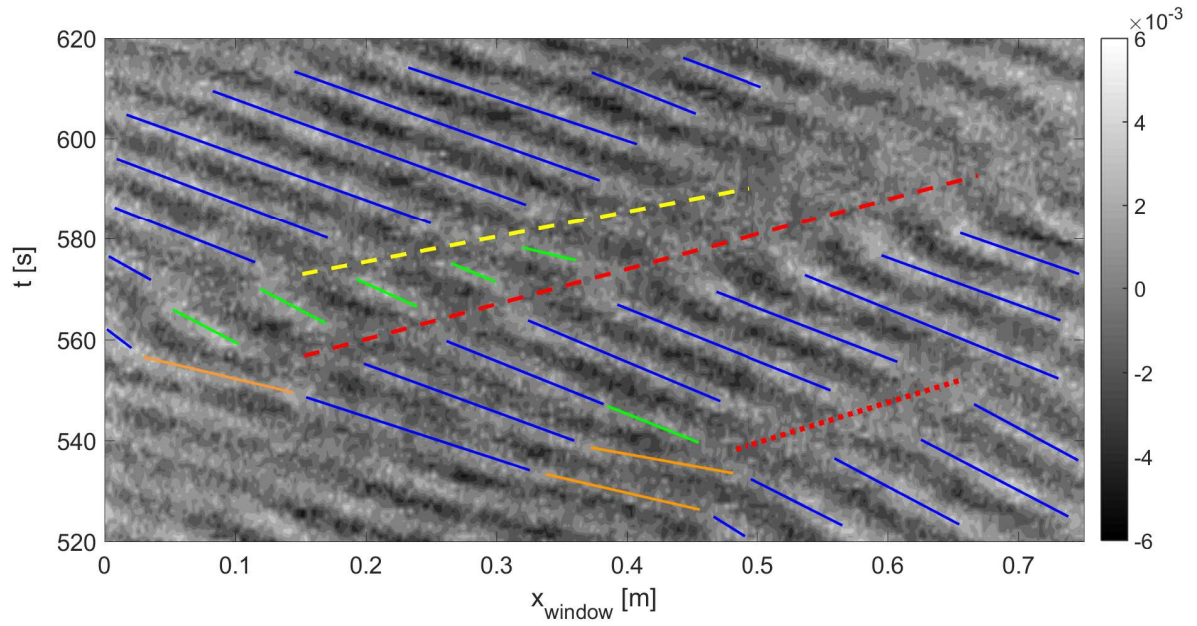


**Figure 11.** Contour plot of the bed elevation perturbation  $Z(x,t)$  during E2 (100 s). The solid blue lines represent the approximated crest trajectory of undisturbed antidunes. The solid orange lines indicate the accelerating antidunes whereas the green lines indicate new antidune crests resulting from splitting events or disturbance-related discontinuities. The other thick lines represent: a travelling disturbance with discontinuity of the antidune pattern (long-dashed red), a splitting-related disturbance without persistent discontinuity (short-dashed red) and a secondary discontinuity/rearrangement of the antidune pattern (long-dashed yellow) associated with a previous discontinuity. The colorbar refers to the  $z$  perturbation expressed as [m].

## List of Tables

763			
764	1	Main parameters for the experimental runs E1–E4. . . . .	42
765	2	Summary of mean flow velocity, bed hydraulic radius, Shields numbers and Froude number for the	
766		experimental runs E1–E4. . . . .	43
767	3	Main parameters of the experimental run <i>2deg15v</i> (Mettra, 2014) and pairs $(c, \lambda)$ based on data of	
768		the same experiment. The pairs $(c, \lambda)$ were extracted from Figure 6.6 and Figure 6.8 (a) in Mettra (2014).	44
769	4	Summary of the performance assessment of Equation (17) for the run <i>2deg15v</i> (Mettra, 2014). . . . .	45
770	5	Summary of the ranges for the antidune wavelength $\lambda$ (extracted from the spectral distributions) and	
771		estimated values for $\lambda_{\min K63}$ (Eq. (18) considering $\bar{h} = h_0$ ) and $\lambda_{R09}$ (Eq. (14)) (runs E1–E3). . . . .	46

**Table 1.** Main parameters for the experimental runs E1–E4.

Run	Dur. [min]	$\bar{\psi}$ [°]	$q_{s,in}$ [m <sup>2</sup> s <sup>-1</sup> ]	$q_w$ [m <sup>2</sup> s <sup>-1</sup> ]	$h_0 \simeq \langle \bar{h} \rangle$ [m]	$h(\text{range})$ [mm]
E1	77	2.9	$2.0 \cdot 10^{-5}$	$3.1 \cdot 10^{-3}$	0.0083	6.5–9.5
E2	37	3.0	$3.5 \cdot 10^{-5}$	$3.8 \cdot 10^{-3}$	0.0092	7.5–10.7
E3	36	3.1	$4.8 \cdot 10^{-5}$	$4.2 \cdot 10^{-3}$	0.0095	8.0–11.0
E4	47	3.0	$6.1 \cdot 10^{-5}$	$4.8 \cdot 10^{-3}$	0.0104	8.5–12.0

**Table 2.** Summary of mean flow velocity, bed hydraulic radius, Shields numbers and Froude number for the experimental runs E1–E4.

Run	$U = q_w/h_0$ [m s <sup>-1</sup> ]	$R_b$ [m]	$\Theta$ [-]	$\Theta_c$ [-]	$\Theta/\Theta_c$ [-]	$Fr = U/(gh_0)^{1/2}$ [-]
E1	0.37	0.0074	0.085	0.066	1.28	1.31
E2	0.41	0.0083	0.095	0.067	1.43	1.38
E3	0.44	0.0086	0.105	0.068	1.55	1.44
E4	0.46	0.0093	0.108	0.067	1.62	1.45

**Table 3.** Main parameters of the experimental run *2deg15v* ([Mettra, 2014](#)) and pairs  $(c, \lambda)$  based on data of the same experiment. The pairs  $(c, \lambda)$  were extracted from Figure 6.6 and Figure 6.8 (a) in [Mettra \(2014\)](#).

$W$ [m]	$\bar{\psi}$ [°]	$d_{50}$ [mm]	$\rho_s$ [kg m <sup>-3</sup> ]	$h$ [m]	$Fr$ [-]	$R_b$ [m]	$\Theta$ [-]	$c$ [mm s <sup>-1</sup> ]	$\lambda$ [m]
0.08	2.0	6.25	2690	0.027	1.17	0.024	0.08	0.8	0.20
								1.8	0.30
								2.5	0.40



**Table 4.** Summary of the performance assessment of Equation (17) for the run *2deg15v* (Mettra, 2014).

$c$ [mm s <sup>-1</sup> ]	$\lambda$ [m]	$\lambda_N^*$ [-]	$\bar{q}_{s,meas}$ [m <sup>2</sup> s <sup>-1</sup> ]	$\bar{q}_{s,est}$ [m <sup>2</sup> s <sup>-1</sup> ]	$(\bar{q}_{s,est} - \bar{q}_{s,meas}) / \bar{q}_{s,meas}$ [%]
0.8	0.20	0.78	$7.9 \cdot 10^{-6}$	$6.43 \cdot 10^{-6}$	-18.0
1.8	0.30	1.17		$7.64 \cdot 10^{-6}$	-2.7
2.5	0.40	1.56		$7.60 \cdot 10^{-6}$	-3.3

**Table 5.** Summary of the ranges for the antidune wavelength  $\lambda$  (extracted from the spectral distributions) and estimated values for  $\lambda_{\text{minK63}}$  (Eq. (18) considering  $\bar{h} = h_0$ ) and  $\lambda_{\text{R09}}$  (Eq. (14)) (runs E1–E3).

Run	$\lambda$ [m]	$\lambda_{\text{minK63}}$ [m]	$\lambda_{\text{R09}}$ [m]
E1	0.06–0.20	0.09	0.106
E2	0.08–0.16	0.11	0.122
E3	0.09–0.15	0.124	0.133